Electronic Supplementary Material (ESI) for Dalton Transactions.

Supplementary Information

---

# Effect of different oxide and hybrid precursors on MOF-CVD of ZIF-8 films

---

Alexander John Cruz[a,b,c], Giel Arnauts[a], Martin Obst[a], Dmitry E. Kravchenko[a], Philippe M. Vereecken[a,c], Steven De Feyter[d], Ivo Stassen[a], Tom Hauffman[b], and Rob Ameloot[a,*]

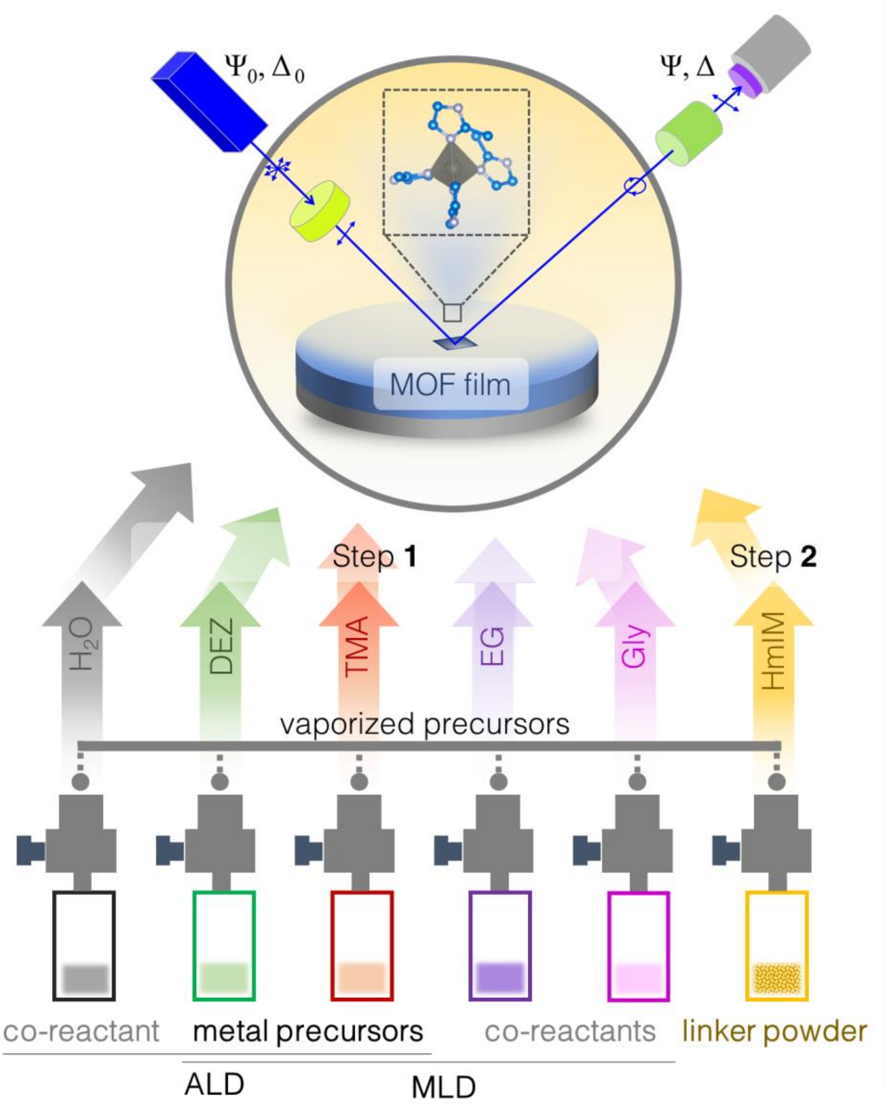

---

[a] Centre for Membrane Separations, Adsorption, Catalysis, and Spectroscopy for Sustainable Solutions (cMACS), Department of Microbial and Molecular Systems ($M^2S$), KU Leuven - University of Leuven, Celestijnenlaan 200F, Leuven, 3001, Belgium; [b] Research Group of Electrochemical and Surface Engineering (SURF), Department of Materials and Chemistry (MACH), Vrije Universiteit Brussel, Pleinlaan 2, Brussels, 1050, Belgium; [c] imec, Kapeldreef 75, Leuven, 3001, Belgium; [d] Division of Molecular Imaging and Photonics (MIP), Department of Chemistry; KU Leuven - University of Leuven, Celestijnenlaan 200F, Leuven, 3001, Belgium

e-mail: rob.ameloot@kuleuven.be

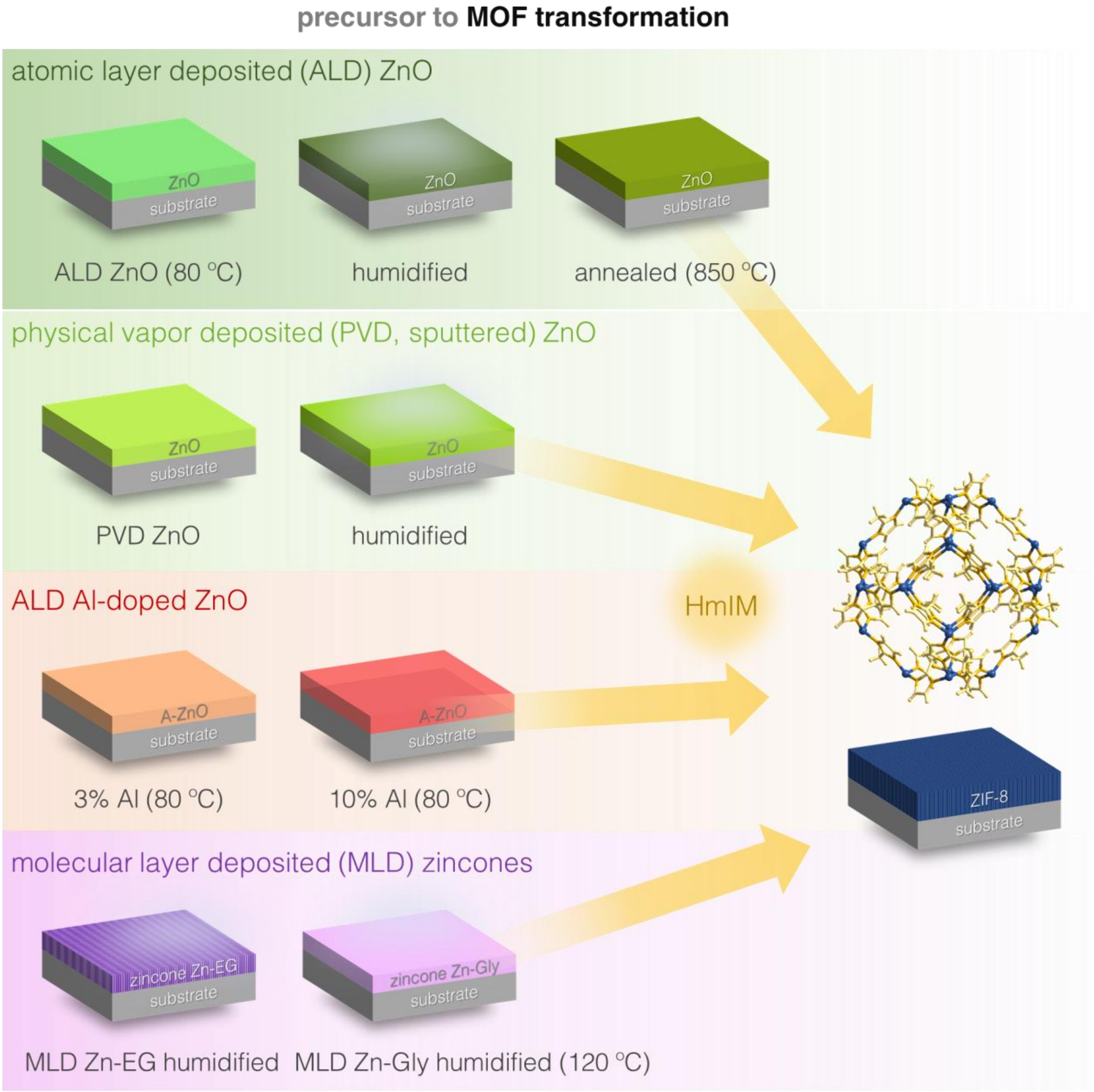

**Figure S1 | MOF-CVD ZIF-8 layers from various Zn precursors.** Various Zn-based films were prepared by atomic layer deposition (ALD)[1], physical vapor deposition (PVD, sputtering), and molecular layer deposition (MLD). These MOF-CVD precursors were subjected to 2-methylimidazole (HmIM) vapor exposure (*i.e.*, conversion to MOF, MOF-CVD Step 2) and yielded ZIF-8 layers.

## Methods

### *Substrates*

200 mm Si wafers (Si-Mat, resistivity = 1-30 Ω · cm, thickness = 725 ± 25 μm) were used. Smaller pieces were cleaved for specific characterization techniques. For the microstructured Si pillar arrays, the Bosch process was used to fabricate these high-aspect-ratio substrates with a diameter of 2 μm and a height of 50 μm. The pillar arrays were separated 2 μm apart in a triangular-pitch geometry and were patterned by standard photolithography procedures with a 600 nm $SiO_2$ as a hard mask.

### ZIF-8 MOF-CVD Step 1a – *atomic layer deposition (ALD) of ZnO*

The ZnO films were deposited using a modified Savannah S-200 thermal ALD reactor (Veeco Instruments, Inc.) with deionized water (DIW) and diethylzinc (DEZ, 97 %, STREM) as precursors. Nitrogen (99.999 %) was the carrier and purging gas used, sourced from a header line in the cleanroom facility. The pulse and purge durations for the ALD precursors were set to 0.015 s and 5 s, respectively. The reactor base pressure was ~ 0.40 mbar at an $N_2$ gas flow of 20 sccm. This process resulted in a ZnO growth rate of 1 Å cycle$^{-1}$ on Si substrates at 80 °C, monitored by *in situ* ellipsometry.

### ZIF-8 MOF-CVD Step 1b - *sputtered ZnO*

Physical vapor deposited (PVD) ZnO films were fabricated using a BAE370 magnetron RF sputter coater with a ZnO target (99.99% purity, Demaco). The depositions took place at a pressure of ~7 ×10$^{-3}$ mbar, under Ar plasma, at a set power of 150 W.

### ZIF-8 MOF-CVD Step 1c – *annealed ALD ZnO*

The annealing process was carried out at 850 °C in air for 2 h. The furnace was preheated before introducing the 3 nm ALD ZnO-coated Si substrates as detailed in Step 1a. The samples were cooled down under an inert atmosphere. This step was carried out to ensure that the ZnO layer will not result in additional moisture exposure, *i.e.*, from the ambient environment, during the cooling step.

### ZIF-8 MOF-CVD Step 1d - *ALD Al-doped ZnO (AZO)*

Using the same reactor as in MOF-CVD Step 1a, a cycle of trimethylaluminum (TMA, 98 %, STREM) and DIW pulses (both at 0.015 s) was inserted for every ***n*** cycles of ALD ZnO, with ***n*** = 15, 10 (**Figure S16**). The presence of Al in the AZO films (as well as in the resulting ZIF-8 layers) was confirmed by X-ray photoelectron spectroscopy measurements (**Figure S17-S18**).

### ZIF-8 MOF-CVD *Step 1e – molecular layer deposition (MLD) of zincones*

The zincone films were deposited using the same cleanroom compatible MOF-CVD reactor (used in Steps 1a, 1b, and 1c). DEZ together with ethylene glycol (EG, 99.5% Acros Organics) and glycerol (Gly, 99+%, Acros Organics) as co-reactants for zinc glycolate (Zn-EG) and zinc glycerolate (Zn-Gly), with precursor canisters heated at 110 °C and 130 °C, respectively. The pulse and purge durations for the DEZ were set to 0.015 s and 10 s, respectively. The purge and carrier gas are $N_2$ at 20 sccm. MLD zincone co-reactants, EG and Gly, were introduced under stop-flow conditions for 30 s, for a pulse duration of 0.15 s. The purge step duration was set to 20 s. This process resulted in a growth rate of 0.8 Å $cycle^{-1}$ and 1.9 Å $cycle^{-1}$ on Si substrates at 120 °C for MLD Zn-EG and Zn-Gly, respectively (**Figure S10-S11**).

### ZIF-8 MOF-CVD *Step 2a - HmIM delivery step, standard protocol, non-humidified conditions*

- ***Start-up operation.*** As detailed in our previous work,[1] the bubbler-type sublimation vessel, initially supplied with freshly-ground HmIM (30 g, 99 %, Sigma Aldrich), was set to 125 °C, while the outlet and supply lines of the bubbler and the connections to the MOF CVD reactor were set to 130 °C and 135 °C, respectively. These connection lines were progressively heated in 30-minute intervals to prevent clogging during start-up. Before the depositions, sequences of purging and drying (100 °C, 30 min) were implemented to ensure the removal of air and moisture in the headspace of the bottle and the HmIM powder bed.

- ***HmIM delivery.*** The $N_2$ flow was stopped and the outlet valve was closed to ensure controlled HmIM delivery and saturation (stopped-flow conditions) inside the reactor at an $N_2$ bubbler pressure of 110 mbar. The substrate and reactor wall temperatures were set to 80 °C and 150 °C, respectively, based on previously optimized protocols.[1]

### ZIF-8 MOF-CVD *Step 2b - HmIM delivery step, humidified conditions*

Immediately before dosing HmIM (described above as Step 2a), water pulses were introduced, achieving ~ 12 % RH in the reactor. This value was estimated by noting the pressure increase in the reactor after dosing, divided by the water saturation pressure at the reactor chuck temperature (80 °C).

### ZIF-8 MOF-CVD *activation protocol*

The recipe was terminated with an evacuation step and with the $N_2$ flow maintained at 20 sccm. The dynamic vacuum was maintained, as the substrate temperature was ramped up to 150 °C. This temperature was held briefly until a constant profile is recorded using *in situ* ellipsometry (~ 10 minutes). The described activation protocol was implemented for all depositions in this work unless otherwise specified.

### *In situ and ex situ ellipsometry*

The thicknesses of the deposited layers were measured using an M-2000x spectroscopic ellipsometer (J. A. Woollam Co. Inc., $\lambda$ = 246-1000 nm). For *in situ* measurements, a custom reactor lid with fused silica viewports was used to collect ellipsometry information (Psi and Delta). The raw ellipsometry data were processed by implementing appropriate models as discussed in detail in ref. **1**. Analysis of *ex situ* ellipsometry data was implemented to estimate the leftover ZnO thickness (degree of conversion) after MOF-CVD. The ZnO and ZIF-8 thicknesses are obtained simultaneously as shown in the diagram:

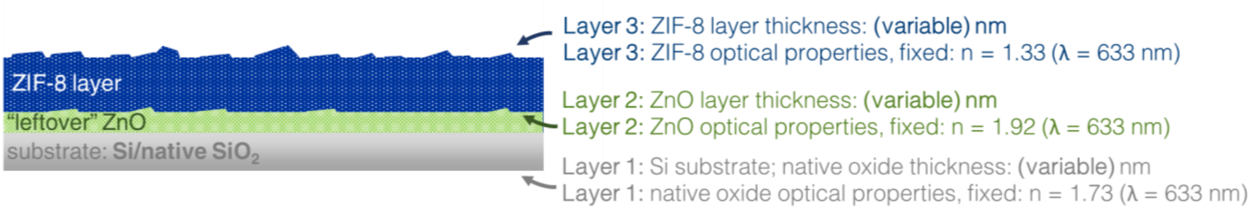

Layer 3: ZIF-8 layer thickness: **(variable)** nm
Layer 3: ZIF-8 optical properties, fixed: n = 1.33 ($\lambda$ = 633 nm)

Layer 2: ZnO layer thickness: **(variable)** nm
Layer 2: ZnO optical properties, fixed: n = 1.92 ($\lambda$ = 633 nm)

Layer 1: Si substrate; native oxide thickness: **(variable)** nm
Layer 1: native oxide optical properties, fixed: n = 1.73 ($\lambda$ = 633 nm)

A three-layer optical model was used consisting of [**i**] a Si substrate with a native oxide layer obtained by measuring the blank wafer; [**ii**] a second layer of (unconverted) ALD ZnO modeled with a general oscillator, and [**iii**] a third layer of ZIF-8 estimated using the Cauchy model. Initially, the optical properties of ZnO (n = 1.92; $\lambda$ = 633 nm) and ZIF-8 (n = 1.33; $\lambda$ = 633 nm) layers were fixed and the thicknesses were varied. No significant differences were observed when the optical properties of the layers were allowed to vary. The % conversion to MOF is estimated by calculating the ratio of the thicknesses of the oxide before and after conversion, assuming that ZIF-8 is the only material formed.

### *Methanol ellipsometric porosimetry*

The samples were placed inside a custom porosimetry chamber and a programmable adsorbate dosing platform. Data were recorded at room temperature, at an equilibration time of 450 s for each data point.

### *Atomic Force Microscopy (AFM)*

Topography images (6 µm × 6 µm and 2 µm × 2 µm, 1024 × 1024 and 512 × 512 pixels) were recorded in intermittent contact mode a PicoSPM 5500 (Agilent Technologies) setup under ambient conditions using Si cantilevers (Olympus, AC160TS-R3). Data analysis was performed using WSXM 5.0 software.[2]

### *X-ray characterization*

Measurements were performed on a Malvern PANalytical Empyrean diffractometer equipped with a PIXcel3D solid-state detector using a Cu anode. Before each measurement, an iterative scheme was employed to optimize both sample height and tilt.

- ***X-ray reflectivity* (XRR)**

  Data were collected between incident angles of -0.03° and 4.5° with a step size of 0.005° and a counting time of 8.8 s.

- ***Grazing incidence*-XRD (GI-XRD)**

  Diffraction patterns were recorded in reflection geometry (incident beam angle 0.2°) within a 5°-45° $2\theta$ range, a step size of 0.053°, and a counting time of 1000 s per step. On the incident beam side, a 1/32° fixed anti-scatter slit was used to limit the divergence of the beam.

***Rutherford Back Scattering* (RBS)**

A 6SDH Pelletron particle accelerator (National Electrostatics Corporation) with a 1.523 MeV He-beam (45 nA) was used to determine the metal density of the MOF-CVD precursors. The scattering and tilt angles were set to 170° and 11°, respectively.

***X-ray Photoelectron Spectroscopy* (XPS)**

XPS data were collected using a PHI Versaprobe II (Physical Electronics) with an Al K$\alpha$ monochromatic X-ray source (photon energy = 1486.71 eV) and a beam irradiation power of 25 W. The kinetic energy of the photoelectrons was measured at a take-off angle of 45°. The vacuum in the analysis chamber was below 1 x $10^{-9}$ Torr during measurements. Survey scans were recorded with a pass energy of 187.85 eV and an energy step size of 0.1 eV. After the identification of the elements of interest using PHI Multipak software (v9.5), high-resolution scans of Zn 2p, C 1s, O 1s, Al 2p, and N 1s were obtained at a pass energy of 23.5 eV and with an energy step size of 0.05 eV. Dual-beam charge neutralization was used to compensate for potential charging effects. The samples exposed to a controlled dose of water vapor exposure (humidified conditions) were immediately transferred to sealed containers filled with inert gas prior to measurements. For the detailed analysis and peak fitting, CasaXPS software (Casa Software, Ltd.) was used, employing a mixed Gaussian-Lorentzian peak shape and a Shirley-type background. The probe depths for the films were found to be 3-5 nm, calculated by multiplying the inelastic mean free path (IMFP) to three and the cosine of the measurement angle for every electron energy of interest. The IMFP was evaluated using the Tanuma, Powel, and Penn (TPP-2M) relation.[3]

***Krypton physisorption***

With a Micromeritics 3Flex 3500 instrument, Kr physisorption isotherm measurements on the MOF coatings deposited on the Si micropillar arrays have been performed as described in detail in our previous works.[1,4–6]

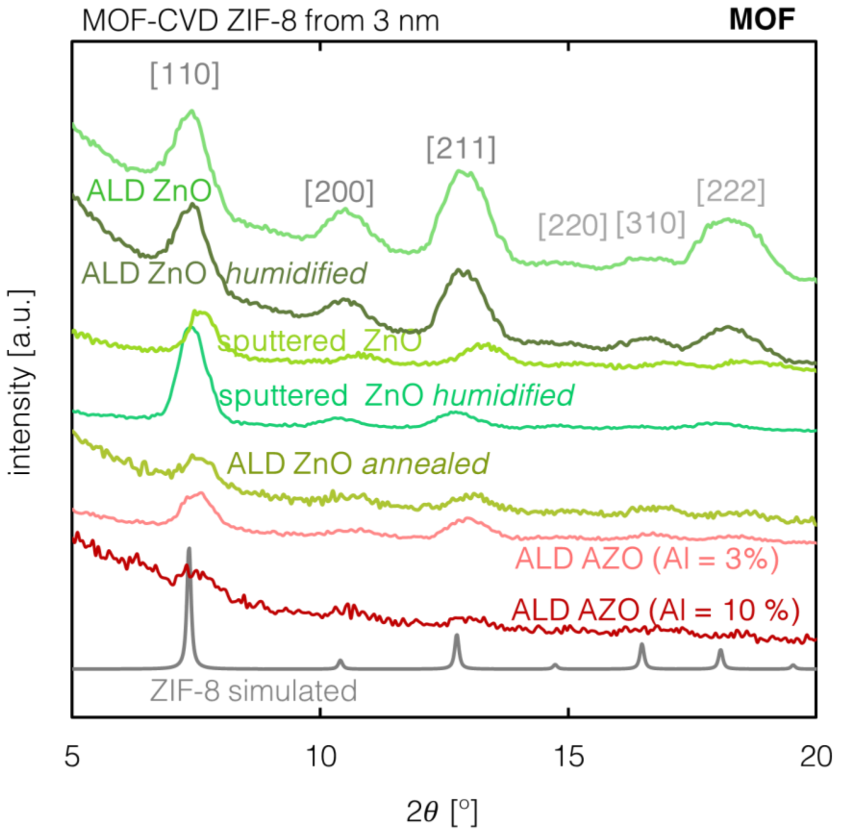

**Figure S2 | MOF-CVD ZIF-8 from different ZnO precursors.**[1] GI-XRD of the MOF layer on Si substrates (CCDC for ZIF-8: VELVOY) recorded with a laboratory diffractometer, implementing a fast measurement routine.

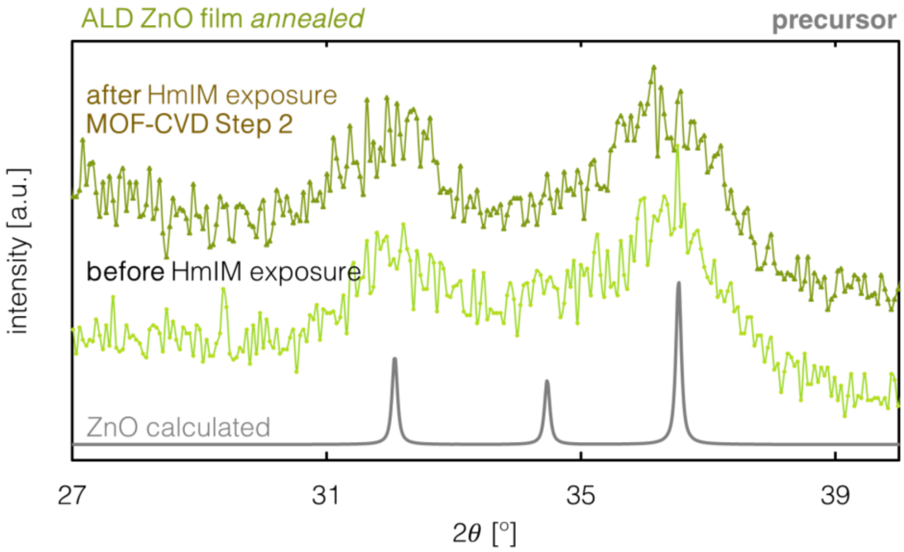

**Figure S3 |** GI-XRD of ALD ZnO after annealing at 850 °C, in air, before (light green) and after (dark green) HmIM exposure (**MOF-CVD Step 2**, see ***Methods***). The presence of ZnO peaks[7] after HmIM linker exposure is attributed to the remaining ZnO.

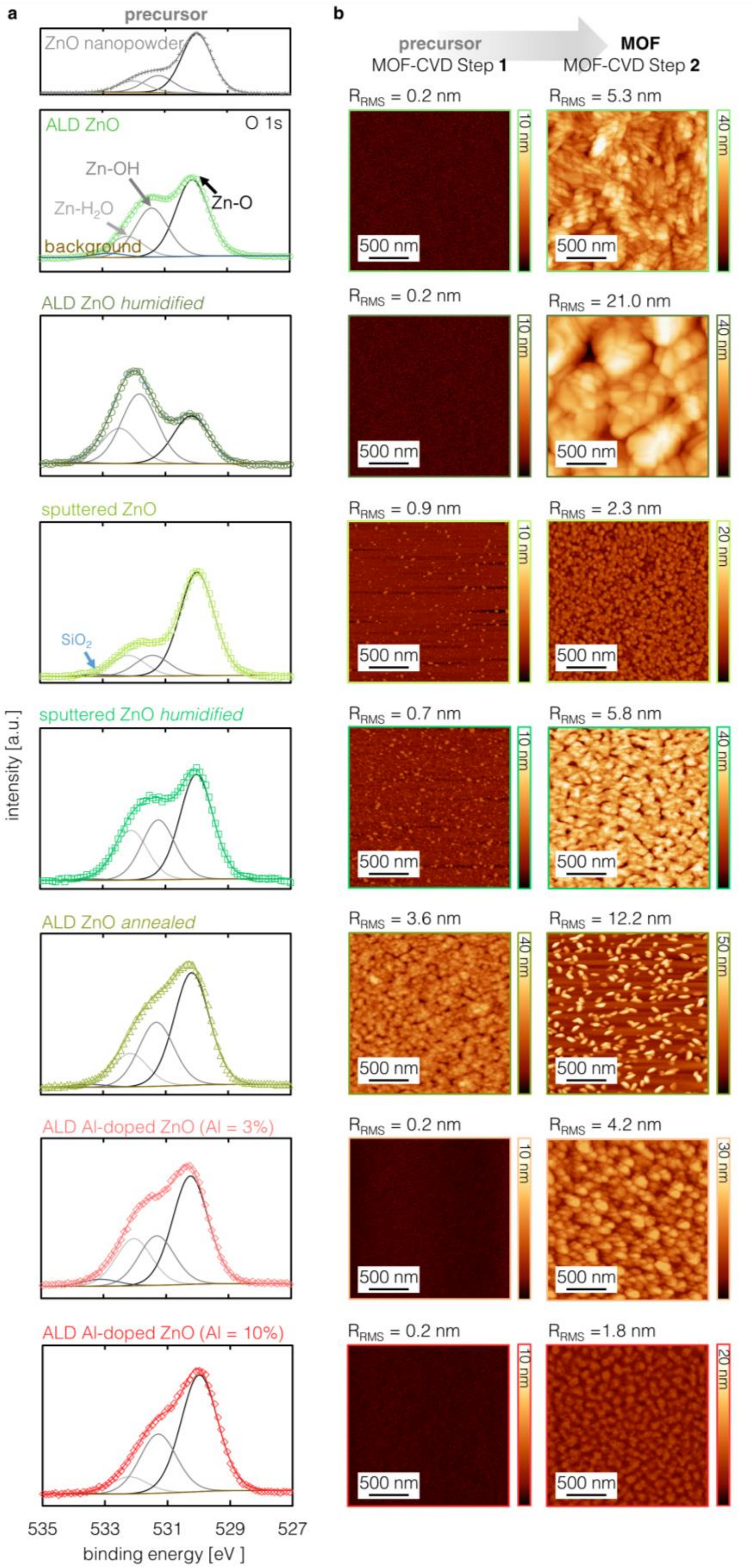

**Figure S4. MOF-CVD ZIF-8 from different ZnO precursors.**[1] **(a)** O 1s XPS of the oxide precursors. **(b)** AFM images of the oxide (ZnO, AZO) and the MOF (ZIF-8). The R$_{RMS}$ values are calculated for a 2 × 2 µm$^2$ probe area. Markers and solid lines represent experimental and fitted data, respectively.

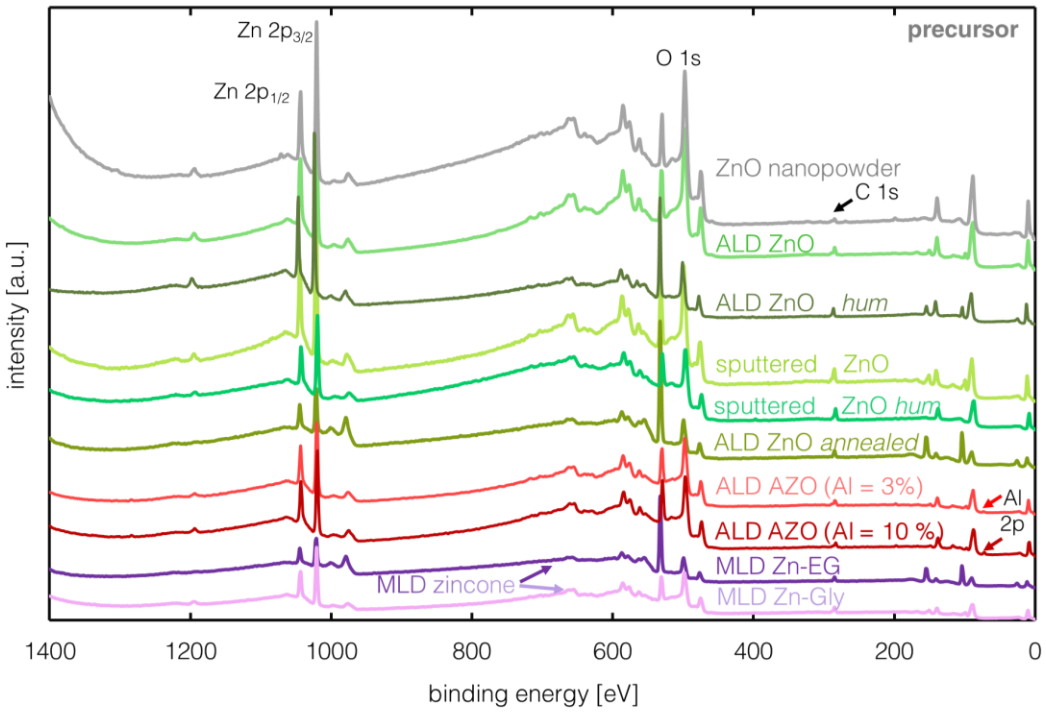

**Figure S5 |** XPS survey scans of the different Zn precursors.

The O 1s XPS of the various ZnO/AZO-coated Si substrates (**Figure S4**) and commercial ZnO nanopowder (≥ 99.5%, Carl Roth, < 25 nm particles) pressed on In foil were analyzed as summarized in **Table S1.**

**Table S1 |** Binding energies (eV) for the components of the O 1s peaks in the different oxide precursors. A reference ZnO nanopowder measurement is included. The full width at half maximum (FWHM, eV) is indicated per sample.

| Assigned components (FWHM, eV) | ALD ZnO as-deposited **(1.3 eV)** | ALD ZnO humidified **(1.3 eV)** | ALD ZnO annealed **(1.2 eV)** | sputtered ZnO **(1.3 eV)** | sputtered ZnO hum. **(1.2 eV)** | ref. ZnO nanopowder **(1.1 eV)** |
|---|---|---|---|---|---|---|
| **Zn-O** | 530.2 | 530.2 | 530.2 | 530.0 | 530.0 | 530.0 |
| **Zn-OH** | 531.7 | 531.7 | 531.3 | 531.4 | 531.2 | 531.2 |
| **Zn-$H_2O$** | 532.3 | 532.3 | 532.1 | 532.2 | 532.1 | 532.1 |
| **$SiO_2$** | 533.5 | 533.5 | 533.5 | 533.2 | 533.4 | n/a |

Peaks with binding energies of 530.0-530.2 eV and 531.2-531.7 eV correspond to Zn-bound $O^{2-}$ and $OH^-$ environments, respectively.[8,9] Another peak, towards the higher binding energy, at 532.1-532.3 eV corresponds to adsorbed water.[9] A low-intensity contribution with a binding energy of 533.2-533.5 eV is attributed to the native oxide on the Si substrate,[10–12] as it would be expected based on the thickness of the ALD ZnO (3 nm) on Si substrates and the calculated probe depth of the XPS equipment (3-5 nm, see *Methods*).

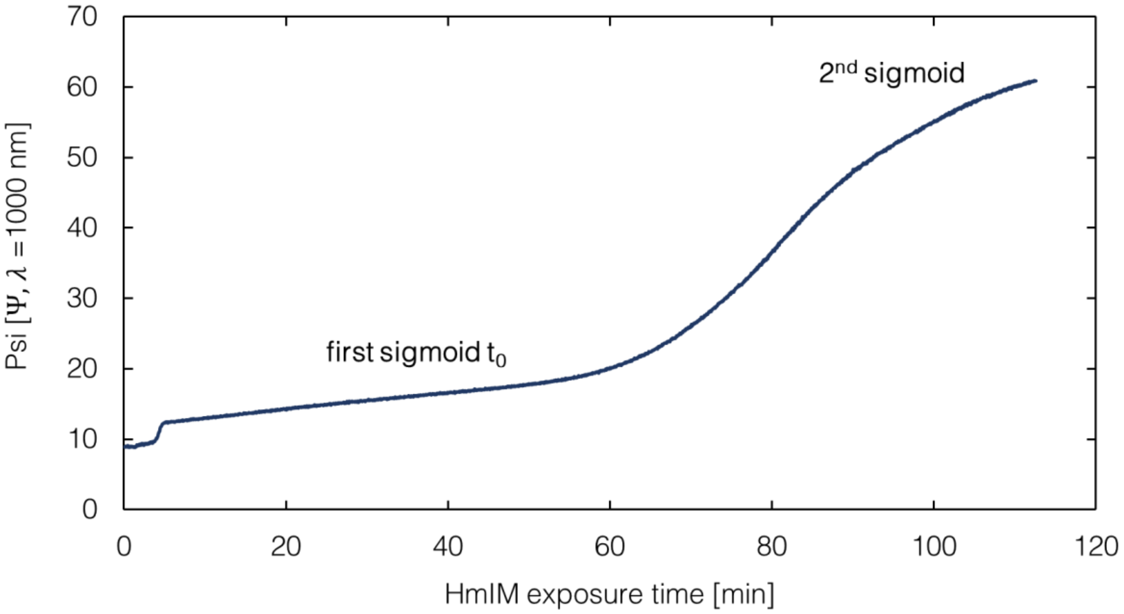

**Figure S6 |** *In situ* ellipsometry data of the transformation of 15 nm ALD ZnO to ZIF-8 under non-humidified conditions. The evolution of Psi (Ψ, $\lambda$ =1000 nm) shows the appearance of a first sigmoidal curve. The duration at which this first sigmoidal curve appears to be stabilizing is referred to as the *characteristic conversion time*, $\mathbf{t_0}$. However, a second, more pronounced thickness expansion is observed after a longer HmIM exposure time. This is likely caused by the formation of the ZIF-8 layer on top of the oxide precursor, slowing down the accumulation of a critical HmIM concentration on the surface/interface. The formed ZIF-8 layer acts as an additional mass transfer resistance layer, thus delaying further reaction and crystallization. This phenomenon is discussed in detail in ref. **1**.

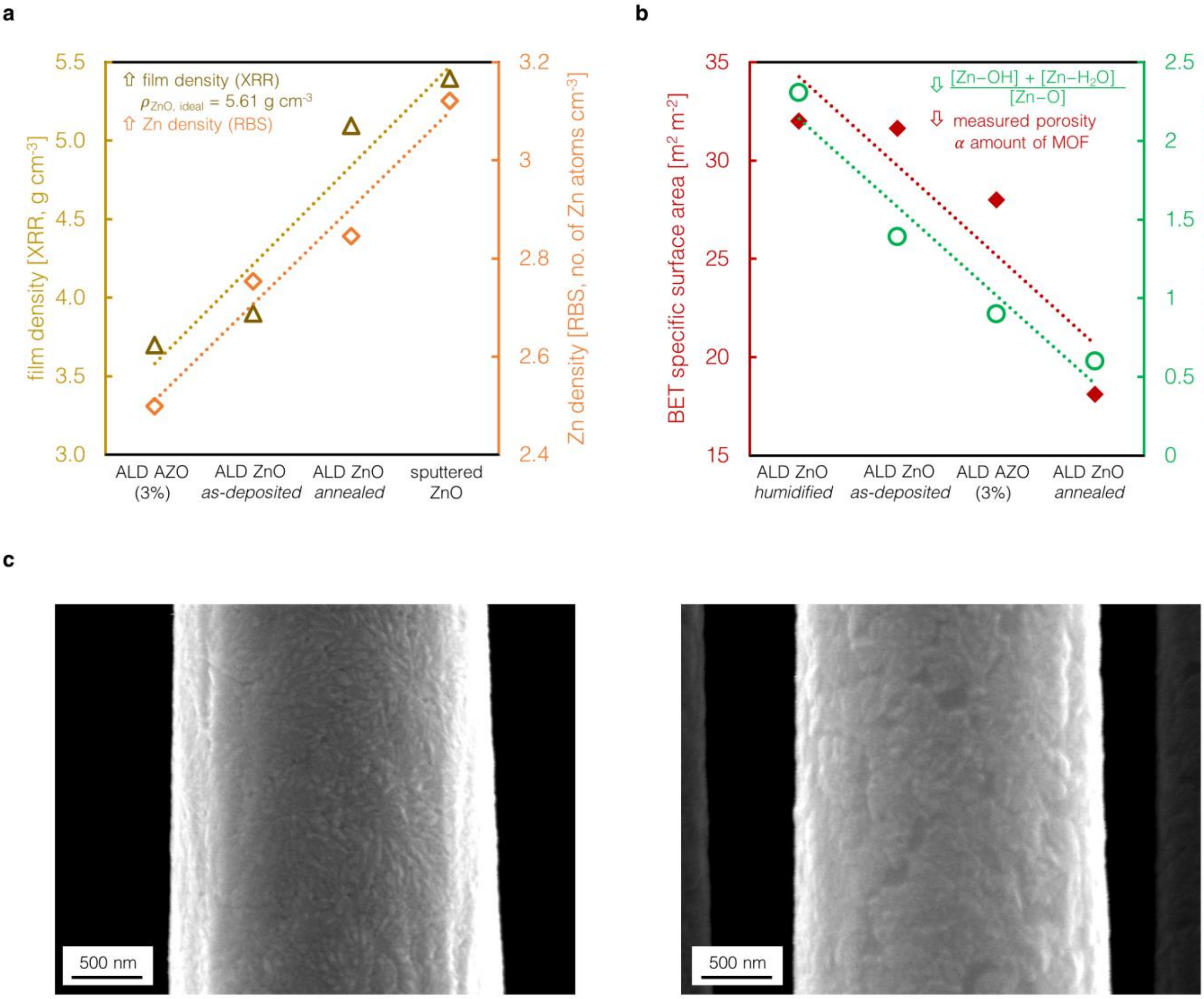

MOF-CVD ZIF-8 from dry conditions

MOF-CVD ZIF-8 from humidified conditions

**Figure S7 |** Relationship of the **a,** film density, and Zn density probed by X-ray reflectivity (XRR, gold triangles) and Rutherford backscattering (RBS, orange diamonds), respectively. **b,** The porosity of the resulting ZIF-8 film by Kr physisorption (solid red diamonds) is related to the hydroxylation degree of the Zn precursor (green circles) and is proportional to the amount of the precursor converted to MOF. The hydroxylation degree (reactivity) and the amount of MOF generated are interrelated parameters. The dotted lines were added to guide the eye. Because of the low thickness of the precursor layers (3 nm), the SEM images of the oxide-coated Si pillars have smooth surfaces without observable features. Here **c,** the SEM images shown are single micropillars after the conversion of ALD ZnO to ZIF-8 under dry and humidified conditions.

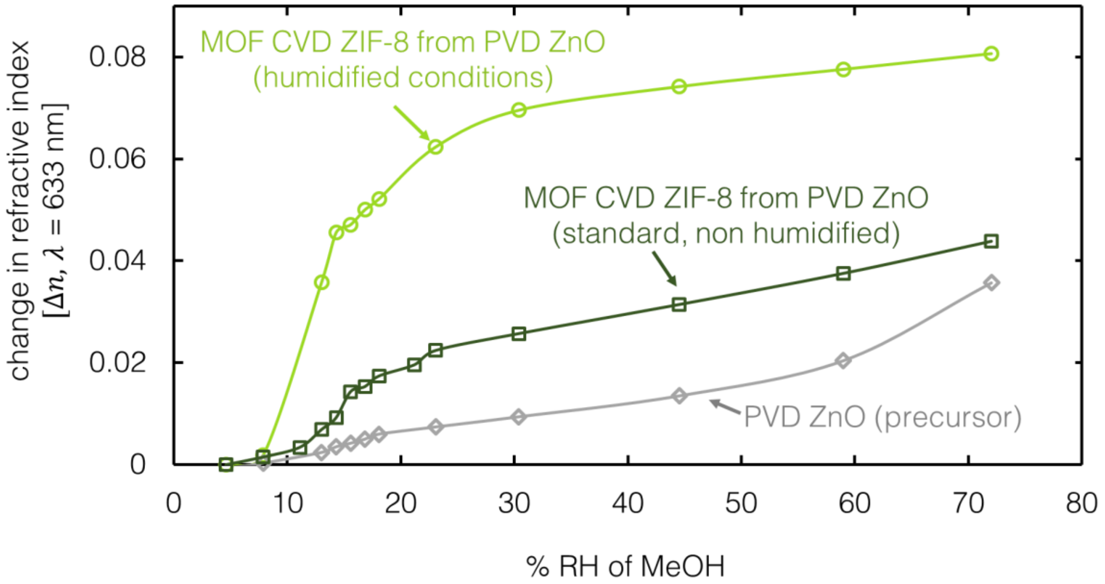

**Figure S8 |** Methanol ellipsometric porosimetry (EP) of MOF-CVD ZIF-8 films on Si, formed from 3 nm PVD ZnO under both non-humidified and humidified conditions (dark green squares and light green circles, respectively). The EP data for the PVD ZnO layer (unconverted, MOF-CVD Step 1, gray diamonds) on Si is included as a reference. The change in the calculated refractive index (detailed in ref. **1,** $\lambda$ = 633 nm) is correlated to the adsorbate uptake. The formed MOF and potentially remaining ZnO precursor were modeled as a single layer.[1,13] Therefore, the refractive index change will be larger when more precursor is converted to MOF. For the ZnO film, The observed refractive index increase at high relative adsorbate pressures is a result of multilayer adsorption. In this case, the shape follows the Type II adsorption isotherm typical for solid non-porous films (precursor = ZnO), different from the Type I curve for microporous materials (MOF = ZIF-8).[14]

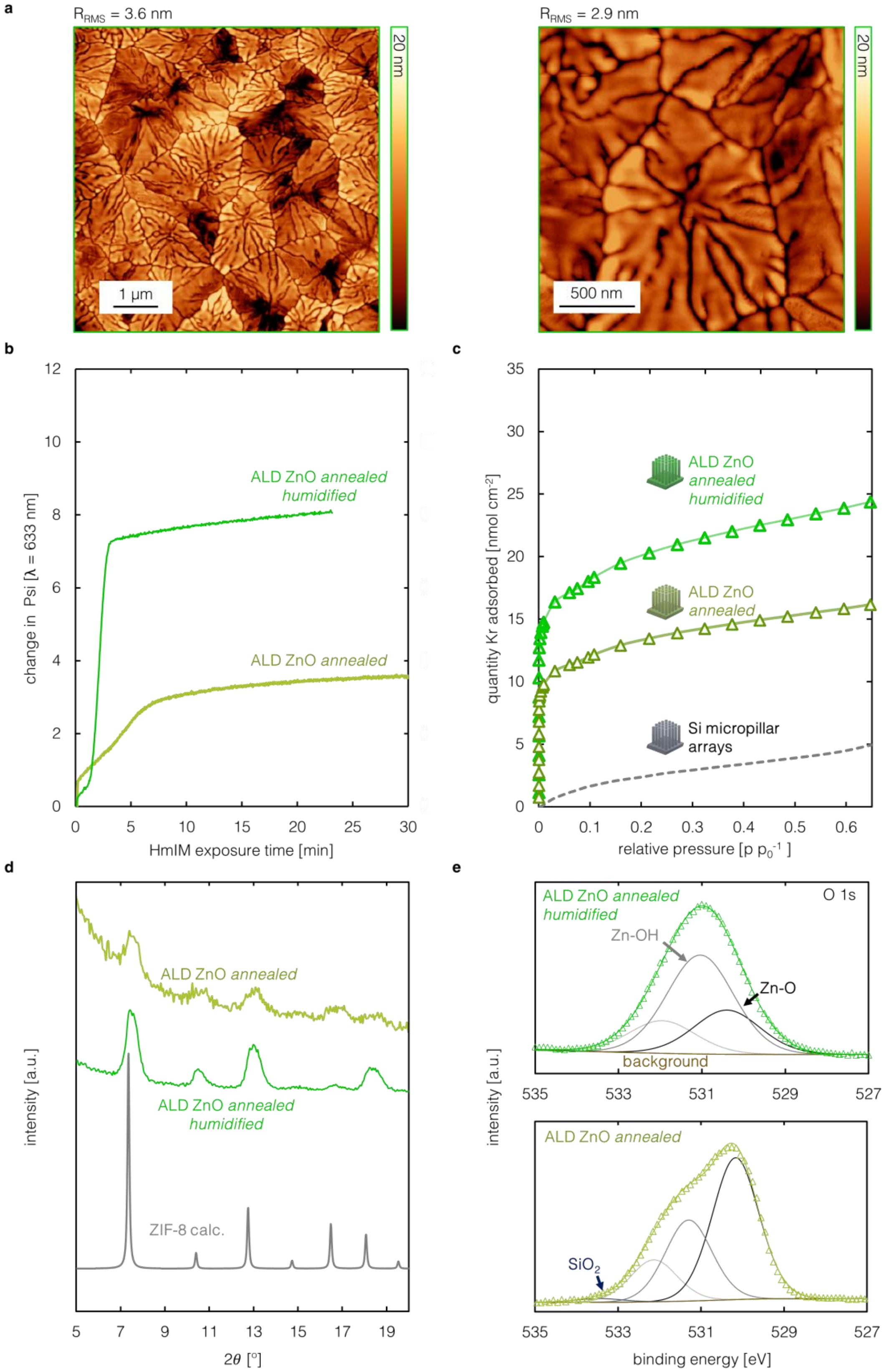

**Figure S9 | MOF-CVD ZIF-8 from annealed ALD ZnO under humidified conditions**. **a**, AFM images (the $R_{RMS}$ values are calculated for a 6 × 6 and 2 × 2 µm$^2$ probe area of the same sample) **b,** *in situ* ellipsometry profile of the oxide-to-MOF transformation **c,** Kr physisorption isotherms of the coating on high-aspect-ratio pillars after the conversion to ZIF-8. **d,** GI-XRD of the resulting ZIF-8 layers (CCDC for ZIF-8: VELVOY). **e,** O 1s XPS (FHWM = 1.8 eV) of the annealed ALD ZnO films both humidified (**top**) and as-prepared (**bottom**, see XPS *data interpretation*, **Table S1**). Markers and solid lines represent experimental and fitted data, respectively.

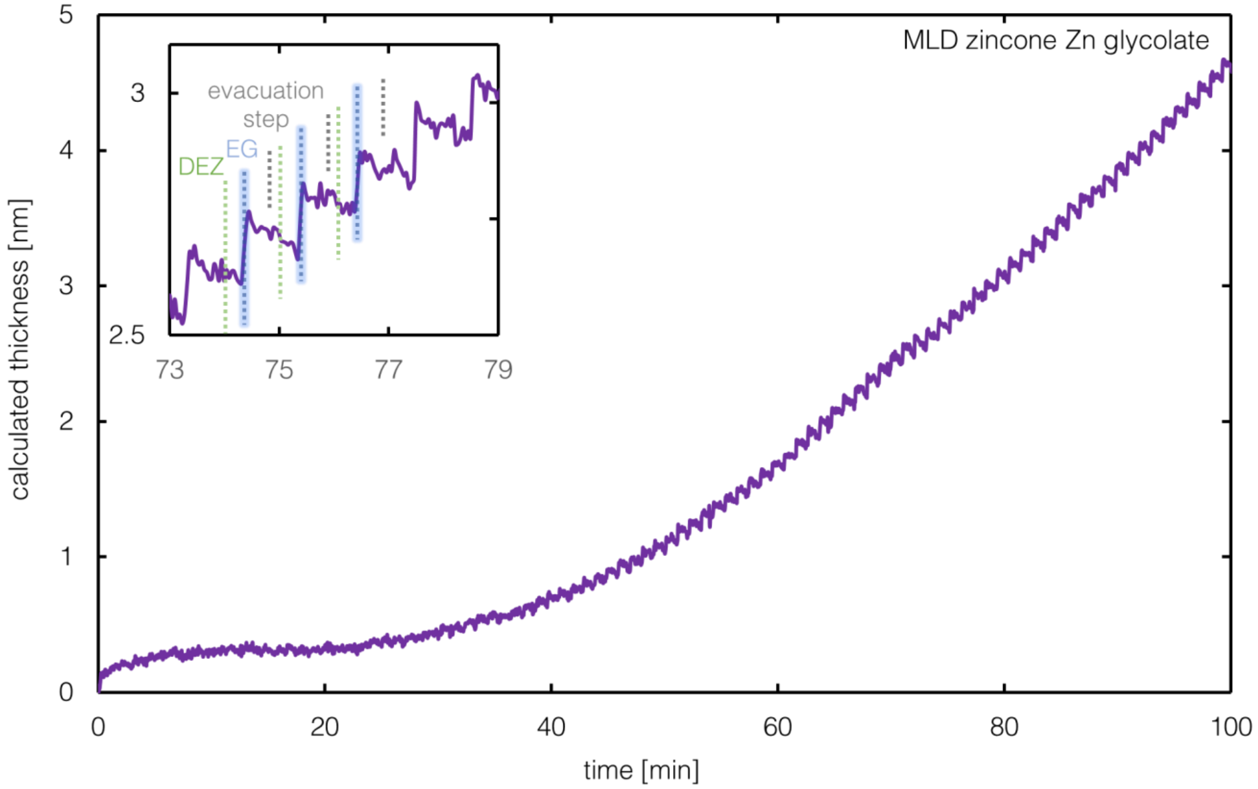

**Figure S10 |** *In situ* ellipsometry monitoring of the molecular layer deposition (MLD) of zinc glycolate (Zn-EG). Ellipsometry data was processed using appropriate models (detailed in ref. **1**). Inset: close-up (6 cycles).

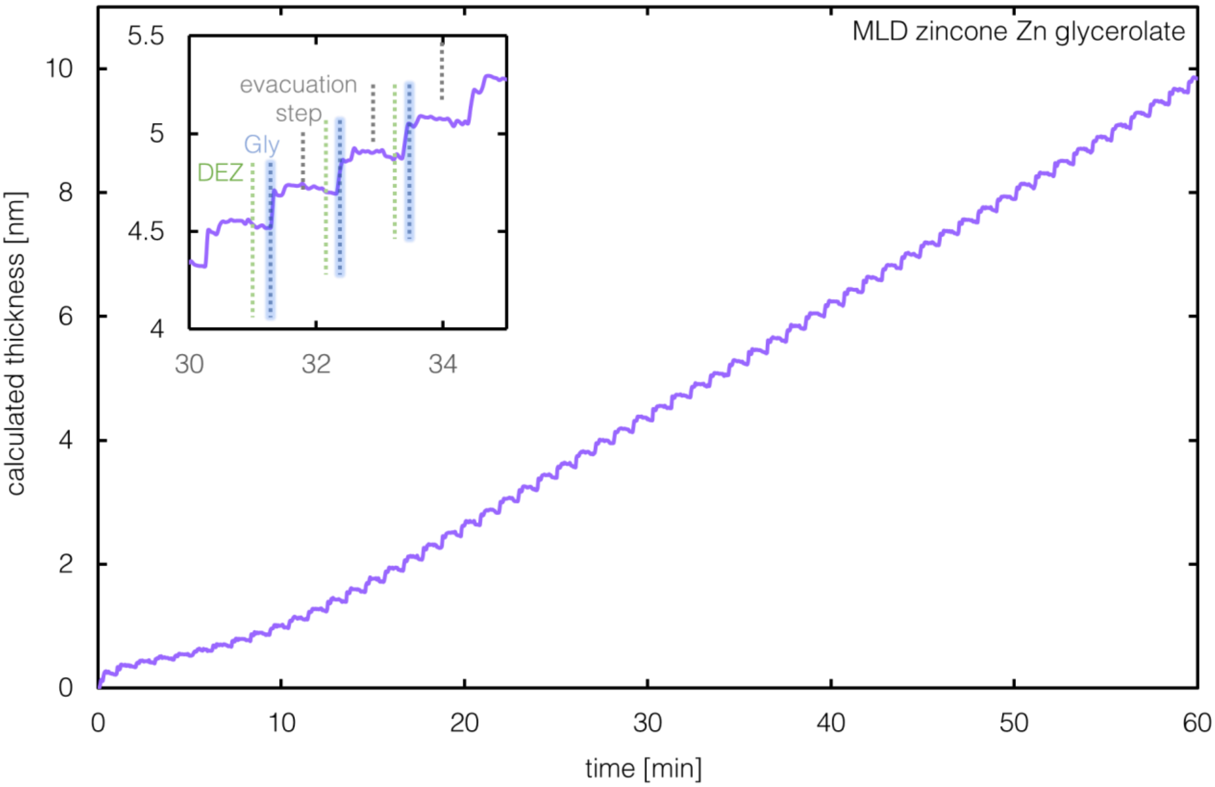

**Figure S11 |** *In situ* ellipsometry monitoring of the molecular layer deposition (MLD) of zinc glycerolate (Zn-Gly). Ellipsometry data was processed using appropriate models (detailed in ref. **1**). Inset: close-up (5 cycles).

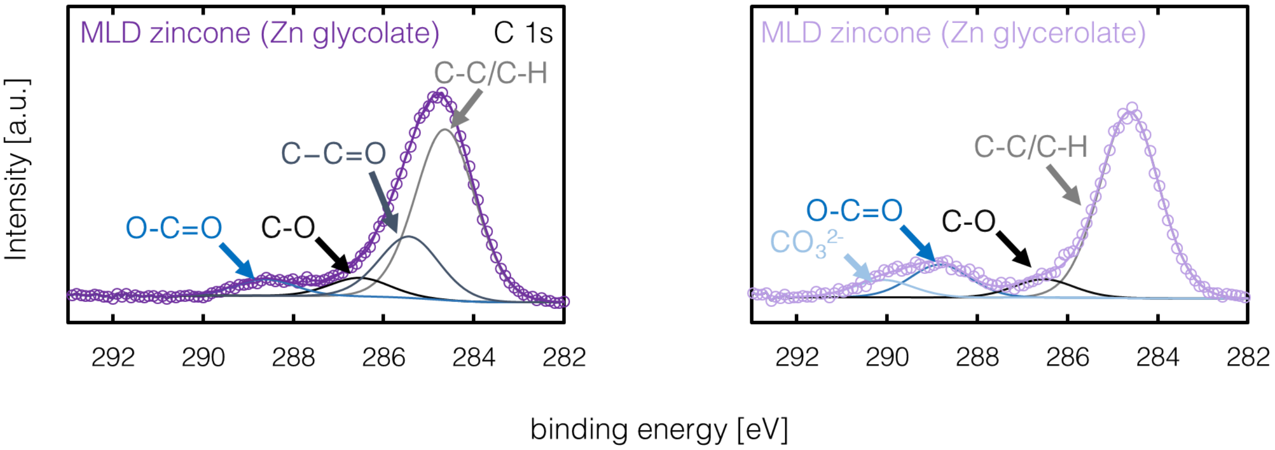

**Figure S12 |** C 1s XPS of a 3 nm MLD zincone layer Zn-glycolate (Zn-EG) and Zn-glycerolate (Zn-Gly) on Si substrates. Markers and solid lines represent experimental and fitted data, respectively.

In the C 1s region, the spectrum of the zincone films (**Figure S12**) can be deconvoluted to multiple C environments based on previous analysis on organic and hybrid polymers.[15–17] For the Zn-glycolate (Zn-EG), the main peak at 284.6 eV (FWHM = 1.6 eV) is assigned to adventitious carbon (C−C/C−H) on the surface and relatively smaller contributions from the beta carbon peak C−C=O (+0.8 eV BE shift with respect to C−C/C−H), C−O (+1.9 eV BE), and O−C=O (+4.1 eV BE). For the Zn-glycerolate (Zn-Gly) the spectrum was deconvoluted to the following components: C-C/C-H at 284.6 eV (FWHM = 1.6 eV), C−O (+1.9 eV BE shift with respect to C−C/C−H), O−C=O (+4.2 eV BE), and $CO_3^{2-}$ (290.1 eV).[18,19]

**Table S2 |** Binding energies (eV) for the components of the O 1s spectra for MLD zincones.

| Assigned components | MLD Zn-EG | MLD Zn-Gly |
|---|---|---|
| Zn-O | 530.4 | 530.1 |
| Zn-OH | 532.4 | 532.0 |
| Zn-OH/O-C=O | 531.6 | 531.2 |
| $SiO_2$ | 533.2 | 533.5 |

The same binding energies for the components in **Table S1** apply, with an additional contribution of O-C=O as shown in previous MLD zincone studies.[15]

15 nm MLD Zn-EG to ZIF-8

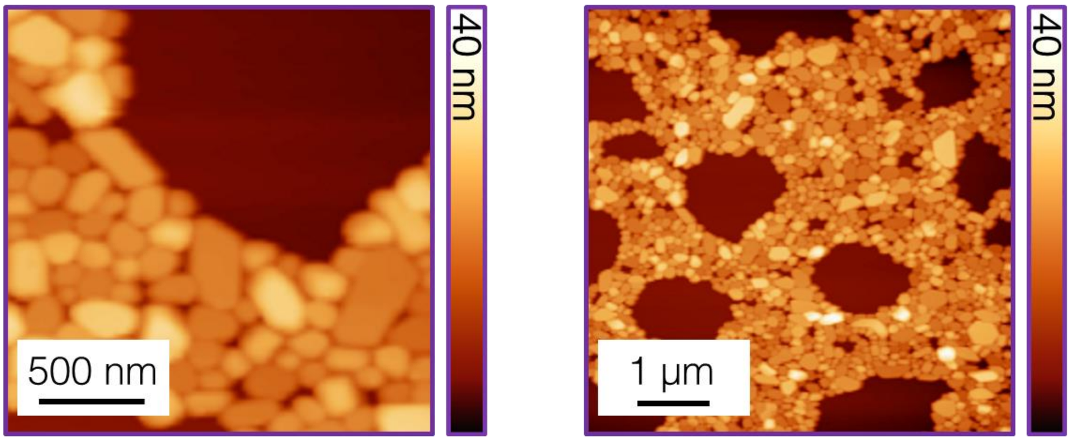

15 nm MLD Zn-Gly to ZIF-8

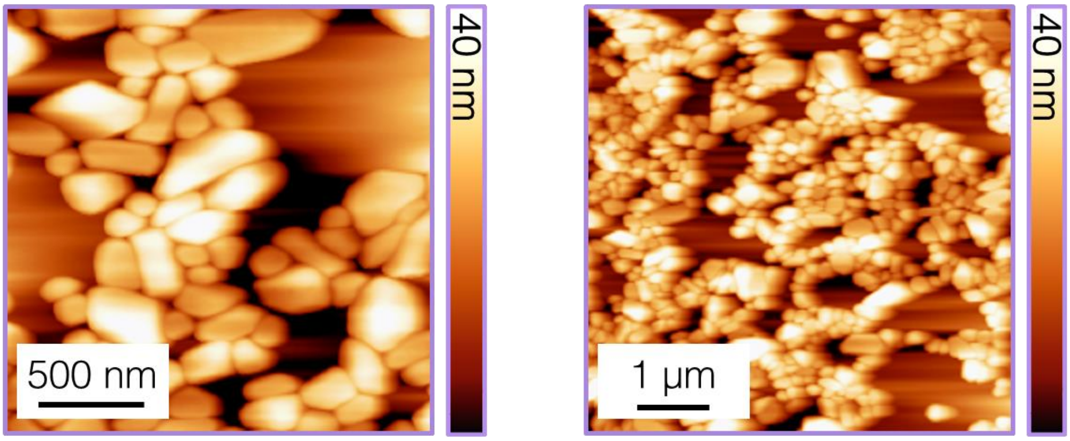

**Figure S13 |** AFM images of the ZIF-8 layers generated from 15 nm of MLD Zn-EG and Zn-Gly using a glass reactor (smaller volume, higher HmIM concentration in the reactive atmosphere with a powder bed as the source of linker vapor, and under non-vacuum conditions, described in detail in ref. **4**).

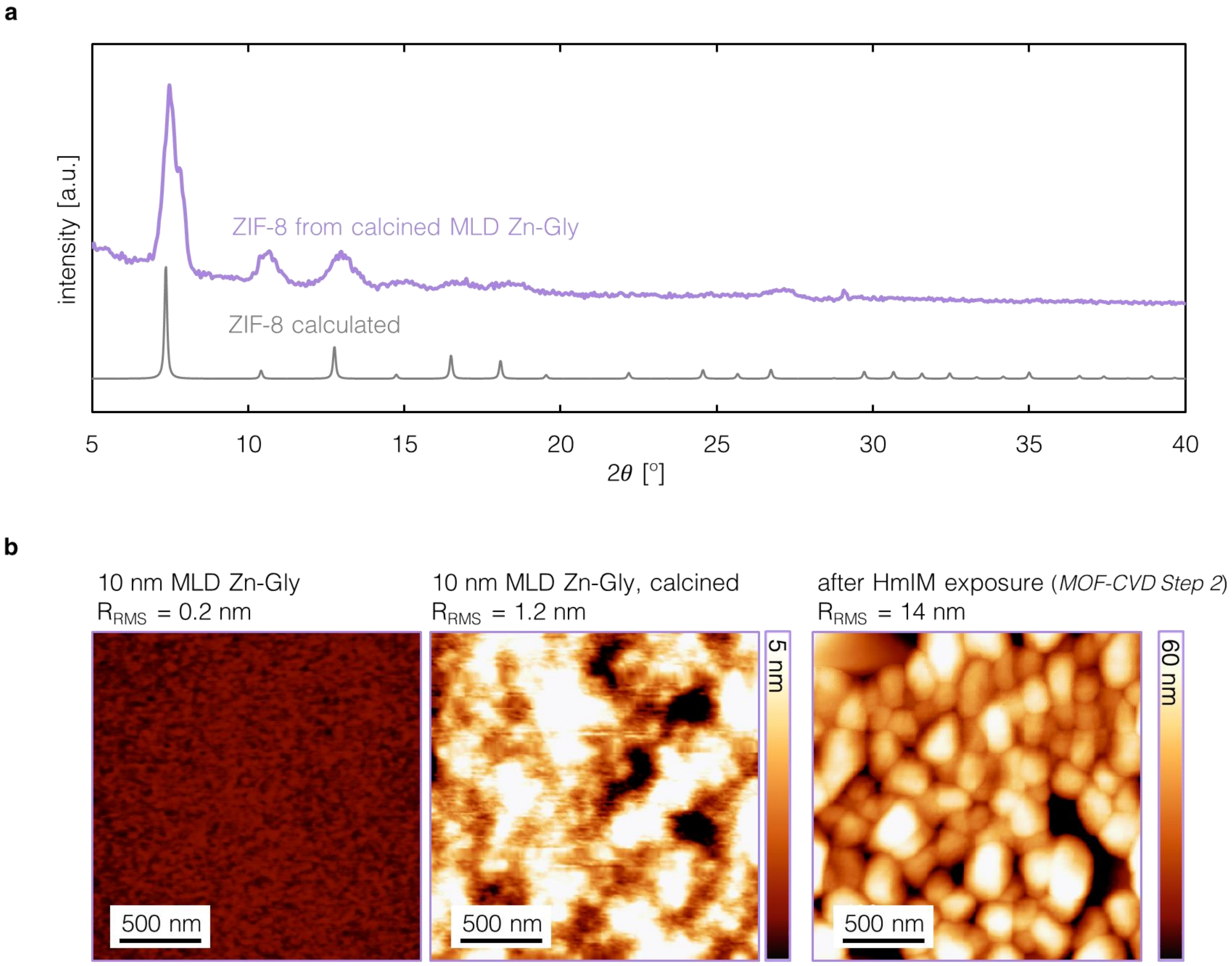

**Figure S14 | a,** GI-XRD of ZIF-8 from calcined MLD Zn-Gly (calcined, 200 °C, in air, 2 h) and converted under humidified conditions (CCDC for ZIF-8: VELVOY). **b,** AFM images of 15 nm MLD Zn-Gly before and after calcination, and after conversion to ZIF-8 under humidified conditions (see *Methods*). The $R_{RMS}$ values are calculated for a $2 \times 2\ \mu m^2$ probe area. The conversions were carried out using glass reactors (vacuum conditions) detailed in previous work.[13]

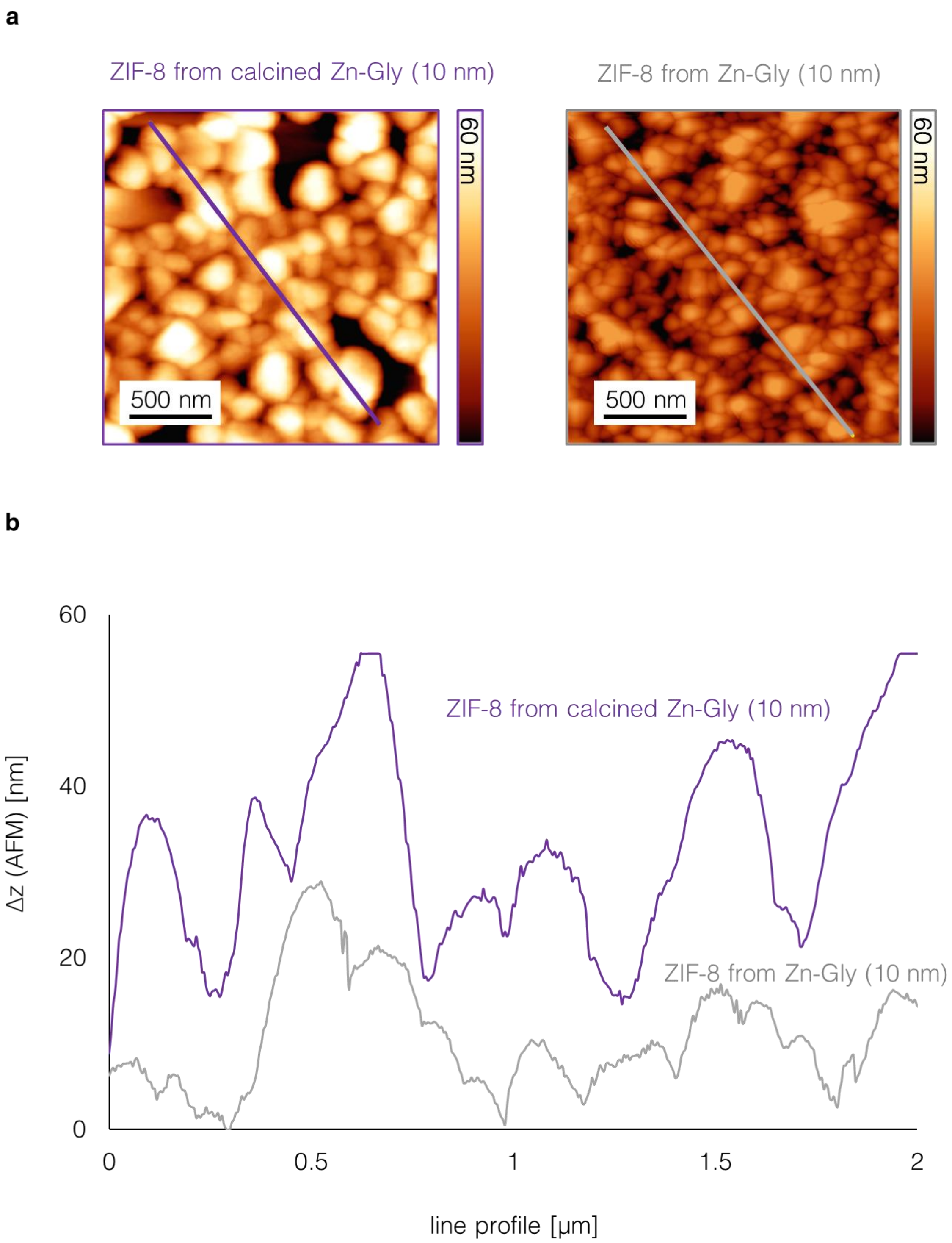

**Figure S15 | a,** AFM images of the ZIF-8 layers generated 15 nm MLD Zn-Gly with (**left**) and without (**right**) a calcination step (calcined, 200 °C, in air, 2 h) under humidified conditions. **b,** Overlay of the representative line profile scans (indicated in **a**) for the ZIF-8 layers from calcined (purple) and as-deposited (gray) Zn-Gly. The conversions were carried out using glass reactors, under vacuum conditions, detailed in previous work.[13]

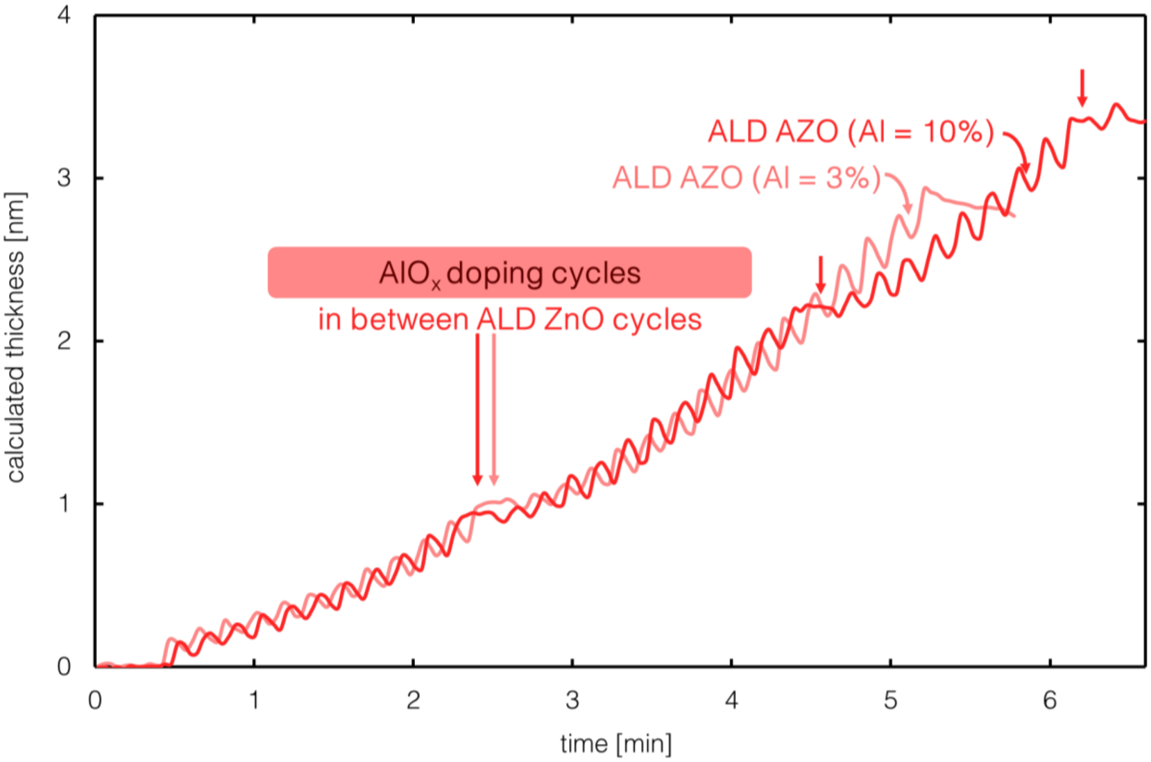

**Figure S16 |** *In situ* ellipsometry of ALD Al-doped ZnO (AZO) for different doping concentrations. The AlO$_x$ doping cycles are introduced/inserted every 15 and 10 ALD ZnO cycles representing 3%, and 10% Al concentration. Al-doped ZnO films are typically used in optoelectronic and photovoltaic device fabrication.[20–23]

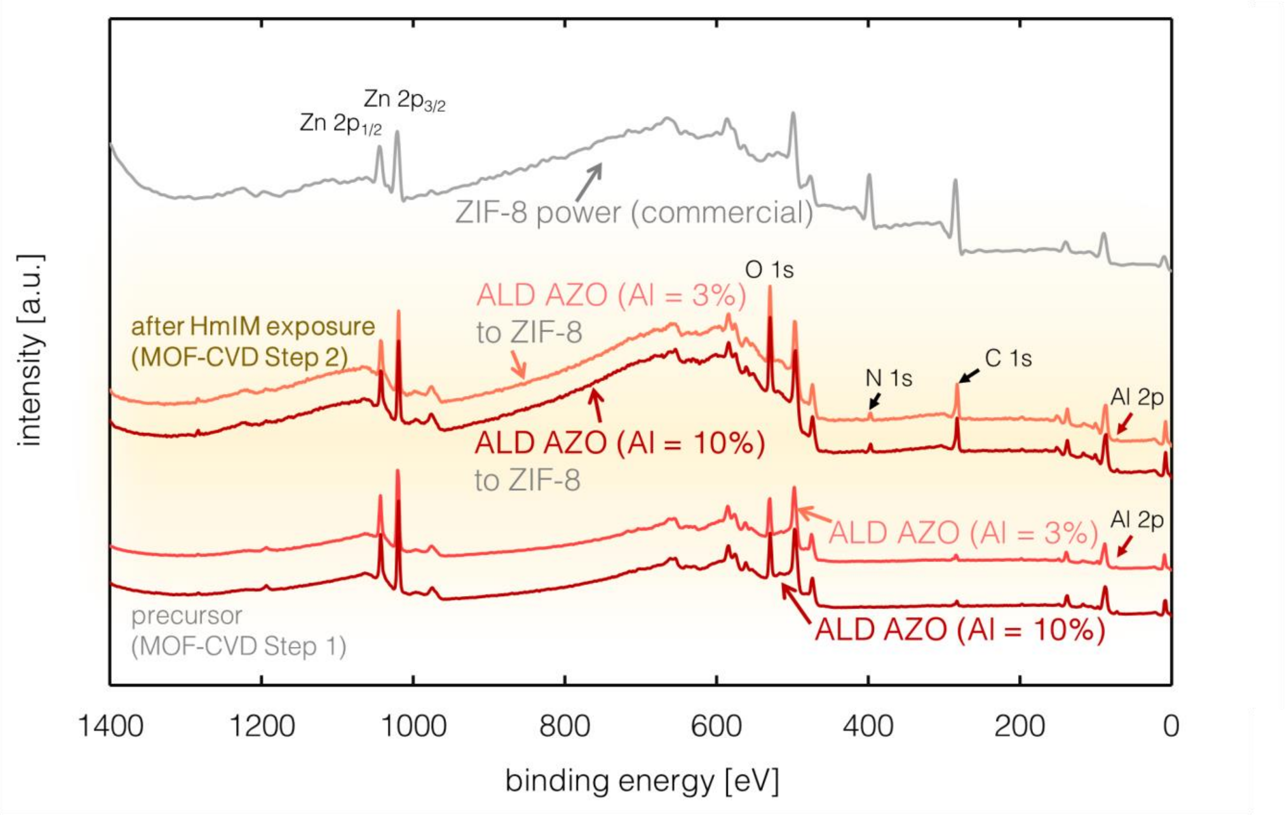

**Figure S17 |** XPS survey scans of the AZO films before and after HmIM exposure. The XPS survey scan of a commercial ZIF-8 powder sample is included as a reference measurement.

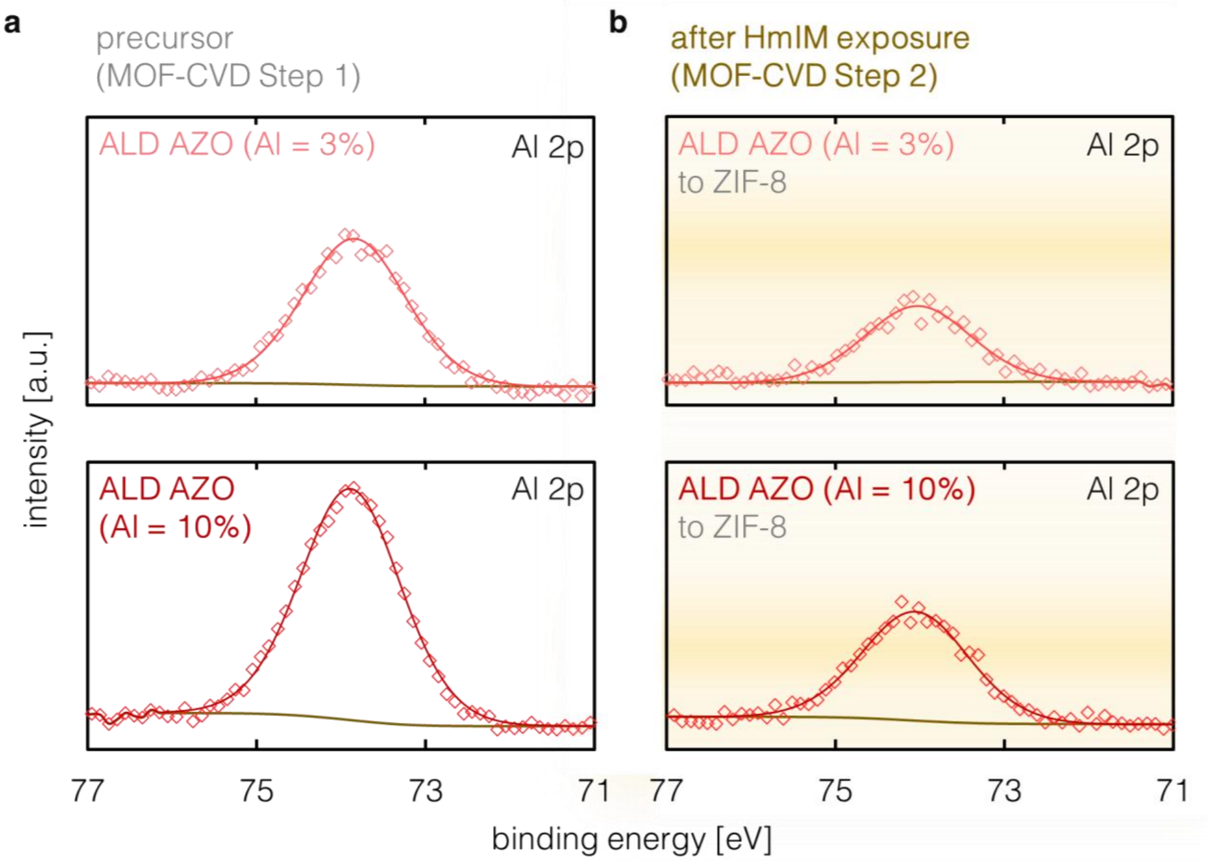

**Figure S18 |** Al 2p XPS of the AZO samples **a,** before, and **b,** after HmIM exposure. The spectra represent a single contribution coming from Al-O, with binding energies of 74.2 and 73.9 eV, and FWHM of 1.5 and 1.4 eV, for the 3 Al % and 10 Al % AZO samples, respectively.[24,25] Markers and solid lines represent experimental and fitted data, respectively.

## Supplementary Information References

1. Cruz, A. J. *et al.* Integrated Cleanroom Process for the Vapor-Phase Deposition of Large-Area Zeolitic Imidazolate Framework Thin Films. *Chem. Mater.* **31**, 9462–9471 (2019).
2. Horcas, I. *et al.* WSXM: a software for scanning probe microscopy and a tool for nanotechnology. *Rev. Sci. Instrum.* **78**, 013705 (2007).
3. Tanuma, S., Powell, C. J. & Penn, D. R. Calculation of electron inelastic mean free paths (IMFPs) VII. Reliability of the TPP-2M IMFP predictive equation. *Surf. Interface Anal.* **35**, 268–275 (2003).
4. Stassen, I. *et al.* Chemical vapour deposition of zeolitic imidazolate framework thin films. *Nat. Mater.* **15**, 304–310 (2016).
5. Tu, M. *et al.* Direct X-ray and electron-beam lithography of halogenated zeolitic imidazolate frameworks. *Nat. Mater.* **20**, 93–99 (2021).
6. Stassin, T. *et al.* Porosimetry for Thin Films of Metal-Organic Frameworks: A Comparison of Positron Annihilation Lifetime Spectroscopy and Adsorption-Based Methods. *Adv. Mater.* 2006993 (2021).
7. Singh, P. *et al.* In situ high temperature XRD studies of ZnO nanopowder prepared via cost effective ultrasonic mist chemical vapour deposition. *Bull. Mater. Sci.* **31**, 573–577 (2008).
8. He, L. *et al.* Fabrication of Au/ZnO nanoparticles derived from ZIF-8 with visible light photocatalytic hydrogen production and degradation dye activities. *Dalton Trans* **43**, 16981–16985 (2014).
9. Woll, C. The chemistry and physics of zinc oxide surfaces. *Prog. Surf. Sci.* **82**, 55–120 (2007).
10. Gross, T. *et al.* An XPS analysis of different $SiO_2$ modifications employing a C 1s as well as an Au $4f_{7/2}$ static charge reference. *Surf. Interface Anal.* **18**, 59–64 (1992).
11. Aghaei, R. & Eshaghi, A. Optical and superhydrophilic properties of nanoporous silica-silica nanocomposite thin film. *J. Alloys Compd.* **699**, 112–118 (2017).
12. Haranath, D. *et al.* Highly efficient, tunable and bright photoluminescence from hydrophobic silica gel nanoparticles. *J. Mater. Chem.* **21**, 9471–9474 (2011).
13. Krishtab, M. *et al.* Vapor-deposited zeolitic imidazolate frameworks as gap-filling ultra-low-$\kappa$ dielectrics. *Nat. Commun.* **10**, 3729 (2019).
14. Naderi, M. Chapter Fourteen - Surface Area: Brunauer–Emmett–Teller (BET). in *Progress in Filtration and Separation* (ed. Tarleton, S.) 585–608 (Academic Press, 2015).
15. Peng, Q., Gong, B., VanGundy, R. M. & Parsons, G. N. “Zincone” zinc oxide-organic hybrid polymer thin films formed by molecular layer deposition. *Chem. Mater.* **21**, 820–830 (2009).
16. Pletincx, S. *et al.* Unravelling the Chemical Influence of Water on the PMMA/Aluminum Oxide Hybrid Interface In Situ. *Sci. Rep.* **7**, 13341 (2017).
17. Hantsche, H. High resolution XPS of organic polymers: The Scienta ESCA300 database. G. Beamson and D. Briggs, Wiley, Chichester, *Surf. Interface Anal.* **20**, 267 (1993).
18. Diler, E., Rioual, S., Lescop, B., Thierry, D. & Rouvellou, B. Chemistry of corrosion products of Zn and MgZn pure phases under atmospheric conditions. *Corros. Sci.* **65**, 178–186 (2012).
19. Hosking, N. C., Ström, M. A., Shipway, P. H. & Rudd, C. D. Corrosion resistance of zinc–magnesium coated steel. *Corros. Sci.* **49**, 3669–3695 (2007).
20. Luka, G. *et al.* Aluminum-doped zinc oxide films grown by atomic layer deposition for transparent electrode applications. *J. Mater. Sci. Mater. Electron.* **22**, 1810–1815 (2011).

21. Islam, M. N., Ghosh, T. B., Chopra, K. L. & Acharya, H. N. XPS and X-ray diffraction studies of aluminum-doped zinc oxide transparent conducting films. *Thin Solid Films* **280**, 20–25 (1996).

22. Jiang, X., Wong, F. L., Fung, M. K. & Lee, S. T. Aluminum-doped zinc oxide films as transparent conductive electrode for organic light-emitting devices. *Appl. Phys. Lett.* **83**, 1875–1877 (2003).

23. Saarenpää, H., Niemi, T., Tukiainen, A., Lemmetyinen, H. & Tkachenko, N. Aluminum doped zinc oxide films grown by atomic layer deposition for organic photovoltaic devices. *Sol. Energy Mater. Sol. Cells* **94**, 1379–1383 (2010).

24. Prince, K. E., Evans, P. J., Triani, G., Zhang, Z. & Bartlett, J. Characterisation of alumina-silica films deposited by ALD. *Surf. Interface Anal.* **38**, 1692–1695 (2006).

25. Sygellou, L. *et al.* $ZrO_2$ and $Al2O_3$ Thin Films on Ge(100) Grown by ALD: An XPS Investigation. *Surf. Sci. Spectra* **18**, 58 (2012).